Dalton Transactions

PAPER

Perylenediimide-based metal–organic frameworks: structural, electrochemical and spectroelectrochemical characterisation

Joseph O. Ogar,[a,b] E. Stephen Davies,[a] Asia R. Y. Almuhana,[c,d] Sarah L. Griffin, [iD][c] Matthew A. Addicoat, [iD][b] Stephen P. Argent [iD][a] and Neil R. Champness [iD] *[c]

The electrochemical and spectroelectrochemical behaviour of metal–organic frameworks (MOFs) using a perylene diimide (PDI) based ligand is reported. Through suitable functionalisation, a PDI-based ligand is made soluble, allowing successful synthesis of two MOFs in combination with cobalt dicarboxylate paddlewheel secondary building units. Spectroelectrochemical techniques are used to probe the electrochemical and optical behaviour of the MOFs demonstrating that the properties of the perylene diimide are maintained by the MOF, facilitating electrochromic behaviour.

Introduction

The wide impact and topicality of MOFs arises from the ability to adapt their design to modify structure and function through choice of the component building blocks. By combination of reticular chemistry and building block adaptation, MOFs have been developed for myriad applications.[1–4] An interesting direction of research is the development of MOFs that comprise components that are either electronically or optically active which can lead to materials with intriguing properties, including conductivity[5] and fluorescence,[6] which can in turn facilitate applications that use materials that change colour upon an external stimulus, such as sensing[7] or electrochromic[8–13] materials.

An approach to the latter applications is to use organic linkers that undergo colour changes upon an electronically stimulated redox process. In this regard MOFs that contain ligands based on rylene diimides are particularly attractive due to the rich chemistry of such systems and their application in electronic and photoactive materials.[14–16] In the context of MOFs, by far the most studied rylene diimides are naphthalene diimides (NDIs).[17] NDI-containing MOFs have been extensively developed and include seminal examples of electrochromic materials.[10,11] Despite the interesting properties that can be developed using NDI components, alternative rylene

diimide analogues such as perylene diimides (PDIs) present distinct properties. PDIs exhibit similarly robust behaviour as NDIs but combine distinct HOMO–LUMO energy gaps, leading to different electro- and photo-chemical properties and colours, along with greater potential for core functionalisation leading to potential adaptability.[15]

Interestingly, PDIs have received far less attention than NDIs in terms of their incorporation into MOFs.[18] Indeed, the examples of PDI-containing MOFs were only reported recently.[19–29] PDI-containing MOFs have been developed for a variety of applications including photocatalysis,[19–22] photothermal conversion[23] and chromatographic separation.[24] It is interesting to consider why NDI-containing MOFs are widespread, but PDI-containing MOFs are significantly less studied. Of the previous reports of single crystal structures of PDI-containing MOFs, a high proportion employ ligands based on a 1,2,6,7-tetrachloroperylene-3,4,9,10-tetracarboxylic acid diimide core.[19,20,23,26–29] Although the other reported examples use ligands with unsubstituted perylene cores, the use of the tetrachloro-PDI, which has a twisted perylene moiety, suggests a primary reason that PDI-MOFs are less studied than their NDI analogues. PDIs exhibit notoriously challenging solubility,[15] primarily due to inter-PDI π–π stacking interactions, and, in combination with solvents commonly used for MOF synthesis such as *N,N'*-dimethylformamide (DMF), the growth of PDI-MOF single crystals, or even crystalline material can be a formidable challenge. An elegant example that illustrates this point was reported by Bein *et al.*[24] in which microcrystalline powders of a PDI-containing MOF was prepared using a linker in which the PDI core was not substituted, and hence remained planar. In this study we demonstrate that functionalisation of the imide substituent of the

[a]School of Chemistry, University of Nottingham, University Park, Nottingham, NG7 2RD, UK
[b]School of Science and Technology, Nottingham Trent University, Clifton Lane, NG11 8NS Nottingham, UK
[c]School of Chemistry, University of Birmingham, Edgbaston, Birmingham, B15 2TT, UK. E-mail: n.champness@bham.ac.uk
[d]King Faisal University, P.O. 380, Al-Ahsa 31982, Saudi Arabia

Paper

PDI group with bulky substituents allows enhanced solubility facilitating growth of crystalline MOF materials suitable for characterisation by single crystal X-ray diffraction (SCXRD). Further, we demonstrate the growth of PDI-based MOFs on transparent electrode surfaces that allow (spectro)electrochemical characterisation of the PDI-based MOFs, affording unequivocal interpretation of the phenomena underpinning electrochromic behaviour.
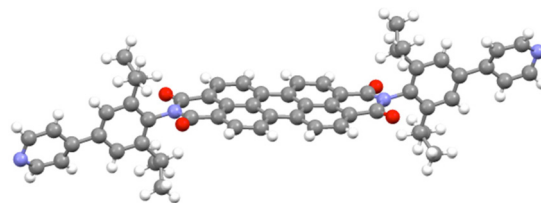

Fig. 1 View of the conformation adopted by L^1 in solid-state crystal structure. Note the distortion from planarity. C – grey; N – blue; O – red; H – light grey.

Results and discussion

To aid the synthesis of PDI containing MOFs, a ligand functionalised with bulky isopropyl groups on the ligands terminal appendages was identified as a way to disrupt PDI-stacking, a feature that typically reduces PDI solubility. Thus, L^1 was prepared as shown in Scheme 1.
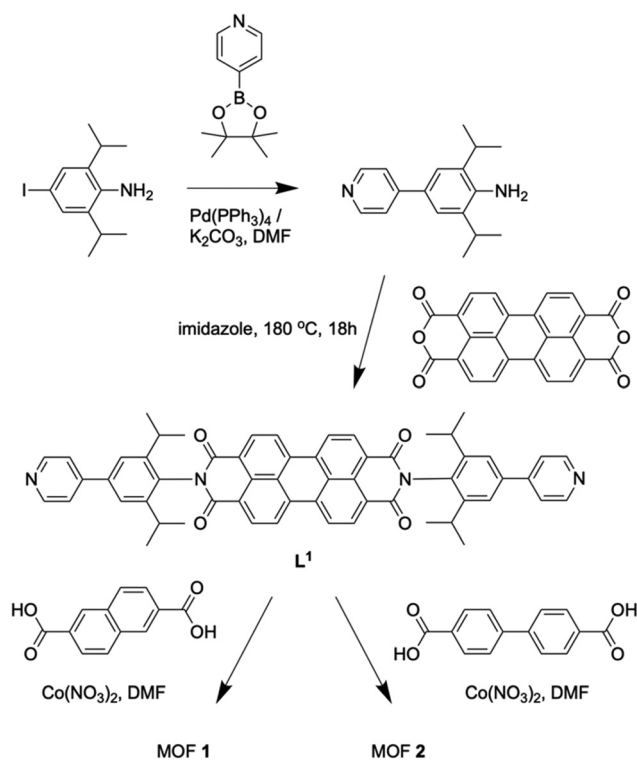
Crystals of L^1 suitable for single crystal X-ray diffraction (SCXRD) studies were obtained by slow evaporation of solutions of the compounds in CH_2Cl_2. Analysis of the single crystal data shows L^1 crystallising in the monoclinic space group $P2_1/c$ (Fig. 1) and reveals that the molecule sits on an inversion centre such that the two halves of the molecule are equivalent. Analysis of the structure shows that the PDI core of L^1 is slightly twisted, with an angle of 7.0° between the naphthyl rings at either end of the perylene core and forms a dihedral angle of 87.5° with the 2,6-diisopropyl-phenyl rings. The twist of the perylene core compares to significantly larger

such angles in other PDI-MOFs, such as 35.2° in a MOF containing 1,2,6,7-tetrachloroperylene-3,4,9,10-tetracarboxylic acid diimide cores.[23]

Two related PDI-containing MOFs, [Co$_2$(2,6-naphthalenedicarboxylate)$_2$(L^1)] (**1**) and [Co$_2$(biphenyl-4,4′-dicarboxylate)$_2$(L^1)] (**2**), were prepared in order to investigate the behaviour of the PDI within a framework material and particularly to probe how the order and organisation of the framework affects the PDI functionality. Both **1** and **2** were prepared by reaction of Co(NO$_3$)$_2$·6H$_2$O, L^1, and the corresponding dicarboxylic acid (biphenyl-4,4′-dicarboxylic acid **1**, or 2,6-naphthalenedicarboxylic acid, **2**) in DMF. Crystals suitable for analysis by SCXRD were grown for **1** and **2** by solvothermal methods.

Crystals of **1** were grown which gave good quality diffraction allowing determination of a 3D MOF structure. Co$_2$(O$_2$CR)$_4$ paddlewheels (Fig. 2a) are linked via the 2,6-naphthalenedicarboxylate ligands into two dimensional sheets, which exhibit the anticipated **sql**-net, and are pillared by the bipyridyl L^1 ligands to create a pillared 3D MOF (Fig. 2b). Topological analysis[30–32] reveals a **pcu** net, a relatively common arrangement in pillared MOFs.[33–35] The MOF adopts a doubly interpenetrated structure (Fig. 2c) leading to more efficient packing; despite this, inspection of the crystal structure reveals that the perylene core of the PDI ligand is considerably curved (Fig. 3b). Rectangular channels in **1**, excluding interpenetration, have dimensions of 32.0 Å by 13.2 Å.

In contrast to **1**, crystals of **2** were weakly diffracting even using a synchrotron X-ray source. Multiple data sets were collected but none gave rise to reliable solutions and therefore it was decided to use a calculated model of a MOF structurally analogous to **1**, i.e. a doubly interpenetrated **pcu** framework, to predict a powder X-ray diffraction (PXRD) pattern for this MOF. PXRD patterns were collected for samples of **2** revealing poor crystallinity for this material (Fig. 3). Comparison of the simulated PXRD data from the calculated MOF structure with the experimental data (Fig. 3) suggests that **2** adopts the same framework structure as **1**. The adoption of a doubly interpenetrated structure is supported by calculations of the energy of interaction between two interpenetrating frameworks of −207 kJ mol⁻¹ (see SI for more details). Considering its poor crystallinity, BET measurements were used to assess the residual porosity of **2** using N$_2$ gas as a probe, which yielded a surface area of 297 m² g⁻¹ indicating that porosity is maintained upon desolvation of the sample.

Scheme 1 Synthetic route to L^1 and MOFs **1** and **2**.

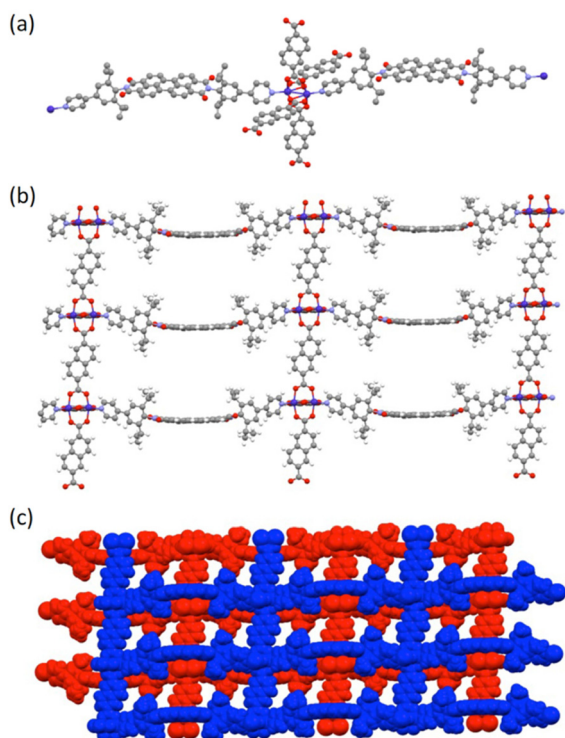**Fig. 2** Views of the crystal structure of **1**. (a) The $Co_2(O_2CR)_4$ paddle-wheel unit observed in **1**; (b) an individual 3D net in which L^1 acts as a pillar linking **sql** nets formed by $Co_2(O_2CR)_4$ paddlewheels and 2,6-naphthalenedicarboxylate ligands, note the significant bowing of L^1; (c) space-filling representation of **1** showing the doubly interpenetrated structure. In (a) and (b): C – grey; Co – dark blue; N – light blue; O – red; H – light grey.
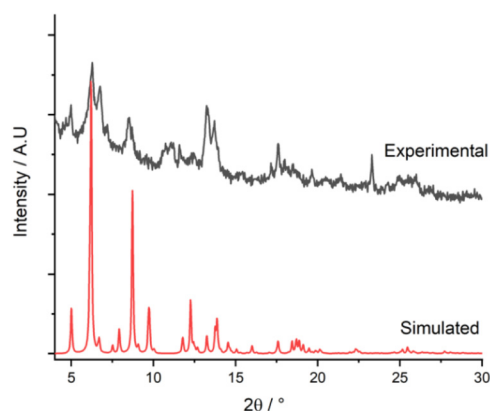

Fig. 3 PXRD patterns for **2**. Experimental pattern (black) revealing poor crystallinity of this sample, and pattern simulated from a calculated model of a doubly interpenetrated **pcu** framework (red).

To investigate the effect of incorporating the PDI moiety into the MOF, electrochemical and spectroscopic measurements were undertaken. For comparison the electronic behaviour of L^1 was studied using cyclic voltammetry (CV), UV-vis spectroelectrochemistry (SEC), electron paramagnetic resonance (EPR) spectroscopy and fluorescence techniques. Most

PDIs are known to exhibit two one-electron reversible reductions,[15,36,37] as determined by cyclic voltammetry, and L^1 is no exception (Fig. S1). UV-visible spectroelectrochemistry (SEC) was used to confirm the reduction of L^1 to its mono- and dianionic forms. The conversion of the neutral compound to the charged delocalised radical monoanion ($L^{1 \bullet -}$) and the interconversion between the mono- and dianionic species, $(L^1)^{2-}$, were successfully probed. $L^{1 \bullet -}$ exhibits intense absorbance peaks at longer wavelengths, as anticipated for PDI monoanions[36,37] and the overall profile for the interconversion between the monoanion and dianion agrees well with those that have been reported previously in the literature[36,37] (see Fig. S3 and Table S1). To further support evidence for the existence of radical anions as probed by the CV and SEC measurements, EPR studies were employed. $(L^1)^{\bullet -}$ produces a complex 23-line EPR spectrum centred at $g_{iso} = 2.0035$ (Fig. S4). The simulated spectra were generated using the parameters listed in Table S2 and matches the experimentally obtained spectra. These data are in good agreement with those reported in the literature for similar systems.[37]

The redox behaviour of **1** and **2** were investigated in the solid-state by cyclic voltammetry, and in the case of **2** transmittance mode UV-vis spectroelectrochemistry. Solid-state CV was performed for **1** and **2** by their encapsulation on the surface of a glassy carbon electrode using a $LiClO_4$ intercalated polyvinylchloride (PVC) matrix.[38,39] For both **1** and **2** CV studies show two reductions (Fig. S2 and Fig. 4 respectively), each assigned as a one-electron process and PDI based, given the similarity in potentials relative to L^1. Hence a PDI moiety incorporated into a MOF framework of **1** and **2** retains the ability to form mono- and di-anionic species. It is notable that the first reduction process occurs at slightly less negative potentials in the case of both **1** and **2** indicating that the first reduction is energetically more favourable when the PDI is incorporated into the MOF rather than in the solution phase (Table 1). Contrastingly the second reduction occurs at very similar potentials whether in a MOF environment or in the solution phase as the free ligand. Although NDI containing MOFs have been studied by electrochemical and spectroelectrochemical methods,[10,11,38–45] the study of PDI-containing MOFs remains unusual, as detailed above.

The cyclic voltammetry for L^1 in solution follows diffusion control. For solid-state **1** and **2** a different response is anticipated. If the MOF were to interact strongly with the electrode surface, for example through chemical modification, then the current would be proportional to scan rate and $\Delta E (= E_p^a - E_p^c) = 0$ V and a pseudo capacitive response would be observed. This is not observed for the experiments with **1** or **2**. Plots of I_p^c or I_p^a versus the square root of scan rate and $\Delta E > 0$ V might indicate that the electrochemical response has a diffusive component (Fig. 4c and d). However, unlike standard diffusion dependent solution phase behaviour, the behaviour observed for the MOFs, a 'diffusion-like' response, may result from either exchange-like electron hopping, as observed in high porosity MOFs featuring large apertures, or counter-ion motion.[46] By comparison with the response for the Fc^+/Fc couple, in solu-
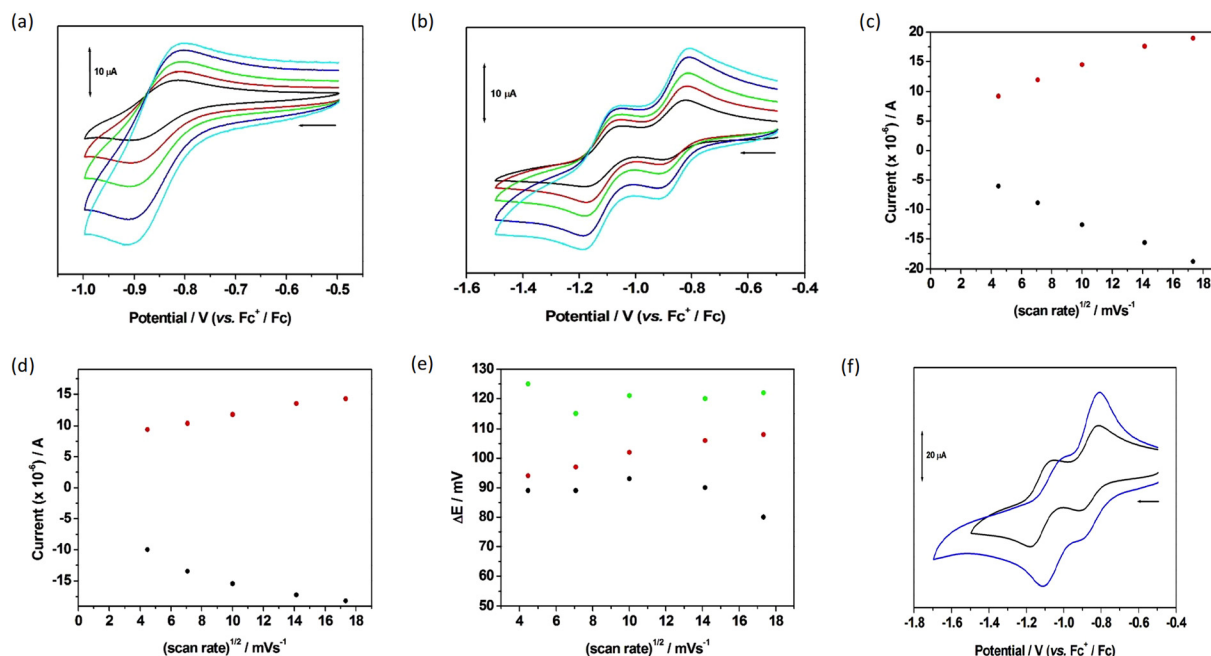
Fig. 4 Solid state cyclic voltammetry of **2** on a glassy carbon electrode using LiClO$_4$ intercalated PVC as supporting matrix in DMF/[Bu$_4$N][BF$_4$] (0.2 M) for (a) the first reduction and (b) second reduction at scan rates of 0.02 (black), 0.05 (red), 0.10 (green), 0.20 (blue) and 0.30 (cyan) V s^{-1}; (c) and (d) plots of the peak anodic current (I_p^a) (red dots) and peak cathodic current (I_p^c) (black dots) *versus* the square root of scan rate for (c) the first reduction and (d) the second reduction; (e) plot of the peak separation, ΔE (= $E_p^a - E_p^c$), for the first reduction (red dots), second reduction (green dots) and ferrocene (in solution) (black dots); (f) initial profile (blue) and stabilised profile (black), at 0.1 V s^{-1}.

Table 1 Cyclic voltammetry for L^1, and MOFs **1** and **2**. L^1 was studied in CH$_2$Cl$_2$ solution using [Bu$_4$N][BF$_4$] (0.4 M) as supporting electrolyte, at 0.1 V s^{-1}. **1** and **2** were studied as solid-state samples on a glassy carbon electrode using LiClO$_4$ intercalated PVC as supporting matrix, in DMF/[Bu$_4$N][BF$_4$] (0.2 M) at 0.1 V s^{-1}. Potentials are quoted *versus* $E_{1/2}$ Fc$^+$/Fc used as an internal standard. Values in brackets are ΔE (= $E_p^a - E_p^c$). E_p^a: anodic peak potential and E_p^c: cathodic peak potential

	1st reduction		2nd reduction		
	CV, $E_{1/2}$/V	SW/V	CV, $E_{1/2}$/V	SW/V	$\Delta E_{1/2}$
L^1	−0.91 (0.07)	−0.91	−1.13 (0.07)	−1.13	0.22
1	−0.85	−0.86	−1.11	−1.13	0.26
2	−0.86	−0.86	−1.12	−1.14	0.26

tion, under these conditions, we note that ΔE (= $E_p^a - E_p^c$) for the MOFs is larger, and increases with increasing scan rate suggesting that the couples all have a component of kinetic control (Fig. 4).[47] It is likely that the electrochemical response results from electron transfers between PDIs located close to the surface, *i.e.* in close proximity to the electrode. The current response to reduction and re-oxidation appears to correlate with the square root of scan rate and this may result from slow electron hopping between PDIs separated by insulating 'metal' layers.[48] It should be noted that the slow diffusion of electrolyte through the pores of the MOFs as a result of ionic interactions or blocked pores may also contribute to this response.[38,49,50] Fig. 4f shows the initial profile and the final

profile of the voltammograms demonstrating a change between the initial and final experiments. We assign this difference to the material not being stabilised on the substrate at the onset of the experiment, but stability is achieved after a few cycles to produce the familiar profile of PDI-based redox processes (Fig. 4a and b).

Samples for SEC studies were grown on fluorine-doped tin oxide glass slides as thin films, using similar conditions to those used for the standard MOF synthesis. In a typical synthesis, the FTO glass slide was washed with alconox and water, then rinsed with acetone followed by ethanol. A monolayer of the carboxylic acid linker[51] was prepared prior to the MOF reaction using 1 mmol of the corresponding dicarboxylate in DMF and heating in the oven at 100 °C overnight. The glass slide was then removed from the solution, rinsed briefly with DMF, and transferred into a 20 mL vial containing a stirred reaction mixture for MOF synthesis (using the same strategy as used for bulk MOF crystallisation). The vial was tightly capped and heated in the oven for 24 h. On completion of the reaction, the vial was removed from the oven and cooled to room temperature. The resulting FTO glass slide was washed with DMF to remove any unreacted starting materials and any crystals that do not adhere strongly to the surface. Further details of experimental design are described in the SI.

It should be noted that the key to a successful measurement of the SEC is formation of a uniform thin film. We were only able to achieve satisfactory sample preparation for **2**, whilst **1** crystallised too quickly to produce a uniform film on

the FTO substrate with large crystallites produced. Thus, our studies focussed on **2**. Spectra recorded for **2** using the SEC approach (Fig. 5) resemble those of the free ligands, L^1. Fortunately, the distinctive features of the spectra observed for **2** and its reduced forms fall within the limits imposed by the FTO glass substrate. The depletion of bands associated with the non-reduced PDI core in **2** to generate a mono-reduced species, $(2)^{\bullet-}$, was the expected pathway for reduction. At the onset of reduction, bands associated with a mono-reduced PDI species were formed, visible as structured features in the 600–900 nm region (Fig. 5b, green line), as bands associated with a non-reduced PDI core, in the 450–550 nm region (Fig. 5b, black line), were depleted. As reduction proceeded, the simultaneous growth of bands associated with both mono and di-reduced PDI species (Fig. 5c) was noted, with the di-reduced PDI identified as intense features in the 500–600 nm region (Fig. 5c, red line). Bands of the mono-reduced species were then depleted in favour of bands characteristic of the di-reduced 2^{2-}, as reduction progressed toward completion (Fig. 5d, blue line). This behaviour differs from that of the PDI precursor, L^1, in solution where distinct generation of mono-

followed by di-reduced species was achieved (Fig. S3). Our inability to generate the spectrum of a distinct mono-reduced species may rationalize the apparent disparity in absorbance for bands of the mono- and di-reduced species in **2** compared to L^1, noting that for the di-reduced MOF, 2^{2-}, the bands appear significantly more intense than those for the mono-reduced species. We hypothesise that the mono reduced species, $(2)^{\bullet-}$, is unstable with respect to 2^{2-} and hence bands associated with this mono-reduced state are not observed in the absence of those associated with **2** or 2^{2-}. Reoxidation reverses the above sequence, with rapid loss of the di-reduced species, the growth and depletion of the mono-reduced species and finally the development of a non-reduced PDI core (Fig. 5e). The difference between the spectral profile obtained before and after the redox cycle is noteworthy (Fig. 5f); the absorbance of the bands associated with the neutral PDI core were less broad, more intense and the baseline position was lower. We interpret this as partial degradation of the film (solid sample remained on the slide following the redox cycle), noting that the electrolyte solution, initially colourless, showed an orange colouration upon completion of the experiment.
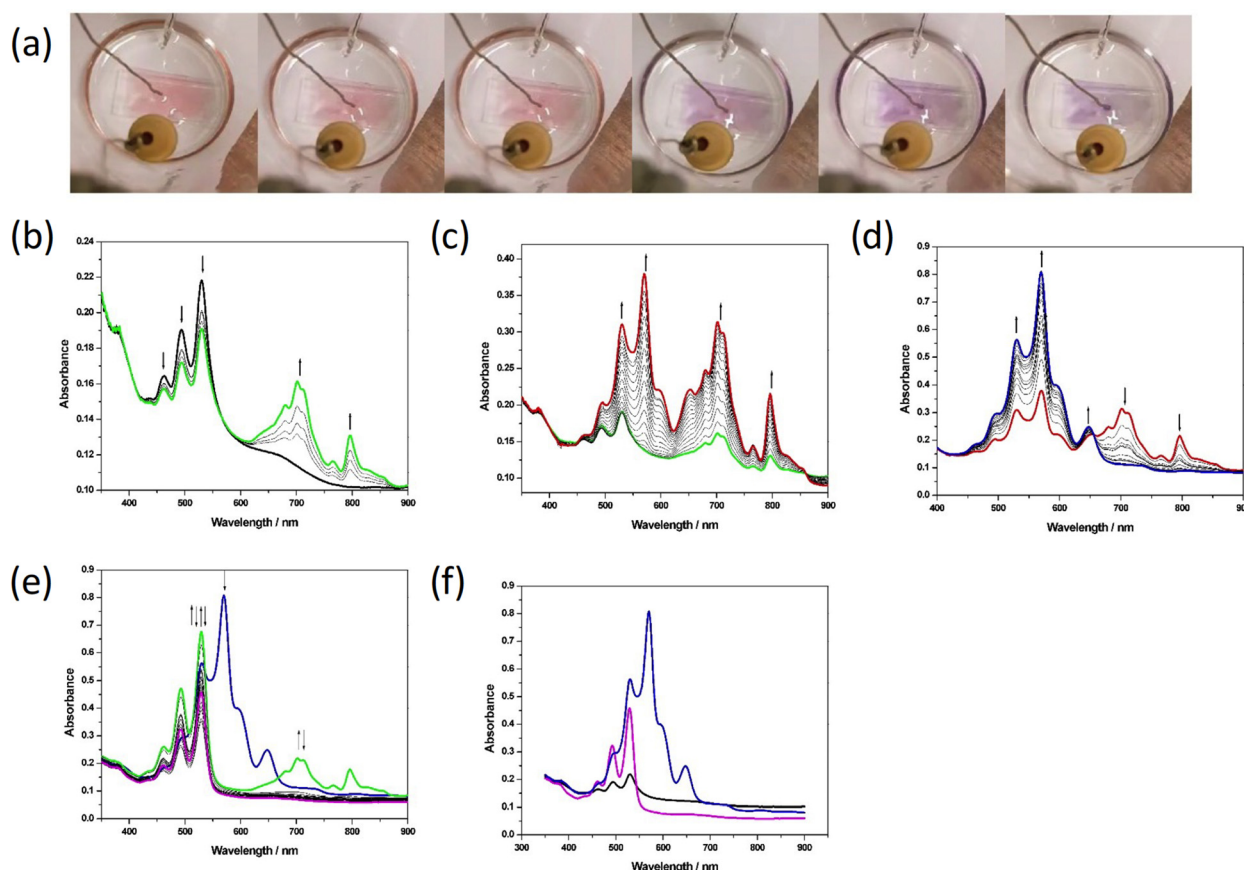

Fig. 5 (a) Colour change observed as a film of **2** is reduced in an electrochemical cell; select images shown, commencing at 0 V (left image) potential swept in 0.1 V steps to −1 V (right image); note change in colour from red to purple upon reduction. UV-vis absorption spectra of **2** showing: (b)–(d) the progress of reduction showing the inter-conversion of redox states between **2** and 2^{2-}; (e) the progress of re-oxidation showing the inter-conversion of redox states between **2** and 2^{2-}; (f) initial spectrum of **2** (black line), 2^{2-} (blue line) and final spectrum of **2** (purple line). Arrows indicate the progress of the stated inter-conversion.

Conclusions

We have successfully demonstrated that PDI-based ligands with sterically bulky substituents can be incorporated into MOF materials, and that the electrochemical and spectroscopic properties of these components are retained allowing electrochromic behaviour to be observed. Spectroelectrochemical measurements confirm that reduced PDI species can be generated electrochemically in thin films of a PDI-based MOF leading to changes in the UV-visible spectrum consistent with mono and di-reduced PDIs. Considering the rich breadth of PDI chemistry[15,36,37,52,53] and the potential for functionalisation our study suggests a path for a large family of electrochromic MOFs using PDI-based ligands.

Conflicts of interest

There are no conflicts to declare.

Data availability

Supplementary information (SI): Synthetic and characterisation methods are described in detail; details of crystallographic analysis and structural modelling; further electrochemical, spectroelectrochemical, EPR, data. See DOI: https://doi.org/10.1039/d5dt02244d.

CCDC 2353806 and 2353807 contain the supplementary crystallographic data for this paper.[54a,b]

Acknowledgements

References

1 K. E. Cordova and O. M. Yaghi, *Mater. Chem. Front.*, 2017, **1**, 1304–1309.

2 A. Kirchon, L. Feng, H. F. Drake, E. A. Joseph and H.-C. Zhou, *Chem. Soc. Rev.*, 2018, **47**, 8611–8638.

3 R. Freund, O. Zaremba, G. Arnauts, R. Ameloot, G. Skorupskii, M. Dincă, A. Bavykina, J. Gascon, A. Ejsmont, J. Goscianska, M. Kalmutzki, U. Lächelt, E. Ploetz, C. S. Diercks and S. Wuttke, *Angew. Chem., Int. Ed.*, 2021, **60**, 23975–24001.

4 S. L. Griffin and N. R. Champness, *Coord. Chem. Rev.*, 2020, **414**, 213295.

5 L. S. Xie, G. Skorupskii and M. Dincă, *Chem. Rev.*, 2020, **120**, 8536–8580.

6 J. Yang, W. Ni, B. Ruan, L.-C. Tsai, N. Ma, D. Shi, T. Jiang and F.-C. Tsai, *ECS J. Solid State Sci. Technol.*, 2021, **10**, 056003.

7 H.-Y. Li, S.-N. Zhao, S.-Q. Zang and J. Li, *Chem. Soc. Rev.*, 2020, **49**, 6364–6401.

8 C. Tao, Y. Li and J. Wang, The Progress of Electrochromic Materials Based on Metal Organic Frameworks. Available at SSRN: https://ssrn.com/abstract=4052318 orDOI: 10.2139/ssrn.4052318.

9 C.-W. Kung, T. C. Wang, J. E. Mondloch, D. Fairen-Jimenez, D. M. Gardner, W. Bury, J. M. Klingsporn, J. C. Barnes, R. Van Duyne, J. F. Stoddart, M. R. Wasielewski, O. K. Farha and J. T. Hupp, *Chem. Mater.*, 2013, **25**, 5012–5017.

10 C. R. Wade, M. Li and M. Dincă, *Angew. Chem., Int. Ed.*, 2013, **52**, 13377–13381.

11 K. AlKaabi, C. R. Wade and M. Dincă, *Chem*, 2016, **1**, 264–272.

12 T. Mitra, A. Summerfield, T. L. Easun, F. Moreau, A. Nevin, C. U. Perotto, E. S. Davies, E. A. Gibson and M. Schröder, *Chem. Sci.*, 2018, **9**, 6572–6579.

13 J. Liu, X. Yun, D. Ma, Z. Wang, L. Xu, T. Xu, C. He, F. Wang and X. Lu, *ACS Appl. Mater. Interfaces*, 2020, **12**, 7442–7450.

14 S. V. Bhosale, M. Al Kobaisi, R. W. Jadhav, P. P. Morajkar, L. A. Jones and S. George, *Chem. Soc. Rev.*, 2021, **50**, 9845–9998.

15 F. Würthner, C. R. Saha-Möller, B. Fimmel, S. Ogi, P. Leowanawat and D. Schmidt, *Chem. Rev.*, 2016, **116**, 962–1052.

16 X. Zhan, A. Facchetti, S. Barlow, T. J. Marks, M. A. Ratner, M. R. Wasielewski and S. R. Marder, *Adv. Mater.*, 2011, **23**, 268–284.

17 Y. Zhou and L. Han, *Coord. Chem. Rev.*, 2021, **430**, 213665.

18 J. Wang, H. Wei, J. Guan, K. Müllen and M. Yin, *Chem. – Eur. J.*, 2025, **31**, e202403234.

19 Z. Liu, C. Li, J. Chen, X. Li, F. Luo, F. Cheng and J.-J. Liu, *Inorg. Chem. Front.*, 2022, **9**, 111–118.

20 S. N. Deger, S. J. Weishäupl, A. Pöthig and R. A. Fischer, *Energies*, 2022, **15**, 2437.

21 Z. Zhong, R. Li, W. Lin, X. Xu, X. Tian, X. Lia, X. Chen and L. Kang, *Appl. Catal., B*, 2020, **260**, 118135.

22 L. Zeng, T. Liu, C. He, D. Shi, F. Zhang and C. Duan, *J. Am. Chem. Soc.*, 2016, **138**, 3958–3961.

23 B. Lü, Y. Chen, P. Li, B. Wang, K. Müllen and M. Yin, *Nat. Commun.*, 2019, **10**, 767.

24 P. I. Scheurle, A. Biewald, A. Mähringer, A. Hartschuh, D. D. Medina and T. Bein, *Small Struct.*, 2022, **3**, 2100195.

25 S. A. Boer, Y. Nolvachai, C. Kulsing, L. J. McCormick, C. S. Hawes, P. J. Marriott and D. R. Turner, *Chem. – Eur. J.*, 2014, **20**, 11308–11312.

26 A. Kumar, J. Li, A. K. Inge and S. Ott, *ACS Nano*, 2023, **17**, 21595–21603.

27 C. Wei, M. Lu, J.-J. Li, Z.-J. Diao, G. Liu, X.-Q. Liu and L.-B. Sun, *J. Mater. Chem. A*, 2024, **12**, 33142–33149.

28 X. Wu, M. Cui, K. Wu, J. Guo, T. Liu, D. Liu, Z. Li, P. Weng, R.-Q. Xia, X. Xiong, Y.-L. Huang, D. Li and J. He, *J. Am. Chem. Soc.*, 2025, **147**, 8350–8360.

29 R. Dalapati, M. Hunter, M. SK, X. Yang and L. Zang, *ACS Appl. Mater. Interfaces*, 2024, **16**, 32344–32356.

30 C. Bonneau, M. O'Keeffe, D. M. Proserpio, V. A. Blatov, S. R. Batten, S. A. Bourne, M. S. Lah, J.-G. Eon, S. T. Hyde, S. B. Wiggin and L. Öhrström, *Cryst. Growth Des.*, 2018, **18**, 3411–3418.

31 V. A. Blatov, A. P. Shevchenko and D. M. Proserpio, *Cryst. Growth Des.*, 2014, **14**, 3576–3586.

32 A. P. Shevchenko, A. A. Shabalin, I. Y. Karpukhin and V. A. Blatov, *Sci. Technol. Adv. Mater.*, 2022, **2**, 250–265.

33 H. Chung, P. M. Barron, R. W. Novotny, H.-T. Son, C. Hu and W. Choe, *Cryst. Growth Des.*, 2009, **9**, 3327–3332.

34 A. Fidalgo-Marijuan, G. Barandika, B. Bazán, M.-K. Urtiaga and M. I. Arriortua, *CrystEngComm*, 2013, **15**, 4181–4188.

35 F. ZareKarizi, M. Joharian and A. Morsali, *J. Mater. Chem. A*, 2018, **6**, 19288–19329.

36 L. Yang, P. Langer, E. S. Davies, M. Baldoni, K. Wickham, N. A. Besley, E. Besley and N. R. Champness, *Chem. Sci.*, 2019, **10**, 3723–3732.

37 N. Pearce, K. E. A. Reynolds, S. Kayal, X. Z. Sun, E. S. Davies, F. Malagreca, C. J. Schürmann, S. Ito, A. Yamano, S. P. Argent, M. W. George and N. R. Champness, *Nat. Commun.*, 2022, **13**, 415.

38 P. M. Usov, C. Fabian and D. M. D'Alessandro, *Chem. Commun.*, 2012, **48**, 3945–3947.

39 S. Rajendran, M. R. Prabhu and M. U. Rani, *Int. J. Electrochem. Sci.*, 2008, **3**, 282–290.

40 B. D. McCarthy, A. M. Beiler, B. A. Johnson, T. Liseev, A. T. Castner and S. Ott, *Coord. Chem. Rev.*, 2020, **406**, 213137.

41 A. M. Beiler, B. D. McCarthy, B. A. Johnson and S. Ott, *Nat. Commun.*, 2020, **11**, 5819.

42 D. K. Panda, K. Maity, A. Palukoshka, F. Ibrahim and S. Saha, *ACS Sustainable Chem. Eng.*, 2019, **7**, 4619–4624.

43 B. A. Johnson, A. Bhunia, H. Fei, S. M. Cohen and S. Ott, *J. Am. Chem. Soc.*, 2018, **140**, 2985–2994.

44 P. W. Doheny, J. K. Clegg, F. Tuna, D. Collison, C. J. Kepert and D. M. D'Alessandro, *Chem. Sci.*, 2020, **11**, 5213–5220.

45 C. Hua, A. Baldansuren, F. Tuna, D. Collison and D. M. D'Alessandro, *Inorg. Chem.*, 2016, **55**, 7270–7280.

46 R. H. Palmer, J. Liu, C.-W. Kung, I. Hod, O. K. Farha and J. T. Hupp, *Langmuir*, 2018, **34**, 4707–4714.

47 S. Brochsztain, M. A. Rodrigues, G. J. F. Demets and M. J. Politi, *J. Mater. Chem.*, 2002, **12**, 1250–1255.

48 H. G. Hong and T. E. Mallouk, *Langmuir*, 1991, **7**, 2362–2369.

49 C. F. Leong, B. Chan, T. B. Faust, P. Turner and D. M. D'Alessandro, *Inorg. Chem.*, 2013, **52**, 14246–14252.

50 C. R. DeBlase, K. Hernández-Burgos, J. M. Rotter, D. J. Fortman, D. dos S. Abreu, R. A. Timm, I. C. N. Diógenes, L. T. Kubota, H. D. Abruña and W. R. Dichtel, *Angew. Chem., Int. Ed.*, 2015, **54**, 13225–13229.

51 S. Roy, Z. Huang, A. Bhunia, A. Castner, A. K. Gupta, X. Zou and S. Ott, *J. Am. Chem. Soc.*, 2019, **141**, 15942–15950.

52 Z. Chen, V. Stepanenko, V. Dehm, P. Prins, L. D. A. Siebbeles, J. Seibt, P. Marquetand, V. Engel and F. Würthner, *Chem. – Eur. J.*, 2007, **13**, 436–449.

53 T. E. Kaiser, H. Wang, V. Stepanenko and F. Würthner, *Angew. Chem., Int. Ed.*, 2007, **46**, 5541–5544.

54 (*a*) CCDC 2353806: Experimental Crystal Structure Determination, 2025, DOI: 10.5517/ccdc.csd.cc2k0b75; (*b*) CCDC 2353807: Experimental Crystal Structure Determination, 2025, DOI: 10.5517/ccdc.csd.cc2k0b86.